Journal of Advanced Ceramics
2019, **8**(3): 333–344
https://doi.org/10.1007/s40145-019-0315-7
ISSN 2226-4108
CN 10-1154/TQ

Research Article

Investigation of magnetoelectric effect in lead free $K_{0.5}Na_{0.5}NbO_3$–$BaFe_{12}O_{19}$ novel composite system

Yogesh KUMAR[a,*], K. L. YADAV[a], Jyoti SHAH[b], R. K. KOTNALA[b]

[a]*Smart Materials Research Laboratory*, *Department of Physics*, *Indian Institute of Technology Roorkee*, *Roorkee 247667*, *India*
[b]*National Physical Laboratory*, *New Delhi*, *Delhi 110012*, *India*

Received: September 3, 2018; Revised: January 8, 2019; Accepted: January 11, 2019

Abstract: Lead-free magnetoelectric composites $(1-x)K_{0.5}Na_{0.5}NbO_3$–$(x)BaFe_{12}O_{19}$ (x = 30, 40, and 50 wt%) are synthesized using solid state reaction method. X-ray diffraction (XRD) patterns confirm formation of diphase composites. Field emission scanning electron microscopy (FE-SEM) gives information about grain size, connectivity, and microstructure of constituent phases. Dielectric parameters of composite samples are studied as a function of temperature and the transition temperatures corresponding to both the constituent phases are observed in the composite samples. Dielectric constant has been found to decrease with addition of ferrite. Room temperature multiferroic behaviour has been confirmed using *P*–*E* and *M*–*H* hysteresis loops and magnetoelectric measurement. Polarization is found to decrease; however, magnetization increases with ferrite weight percentage. The highest α_{ME} of 4.08 mV/(cm·Oe) is obtained for x = 30 wt% composite and it is realized that ferrite content significantly affects magnetoelectric behaviour.

Keywords: composite materials; X-ray diffraction (XRD); microstructure; dielectric; multiferroic

1 Introduction

In this contemporary era of device miniaturization and device multi-functionality, magnetoelectric (ME) composites have enticed the science fraternity towards themselves owing to their large ME coupling with respect to their single phase counterparts. Presence of large ME effect in composite materials has compelled the researchers to exploit their use in diverse applications including: spintronic devices [1,2], high sensitivity magnetic field sensors [3], sensors and transducers [4,5], and electric field controlled ferromagnetic resonance devices [6]. Large scale applications of ME composites given their higher ME coupling than that of single phase materials make them a beguiling research concern. ME coupling in the composites is basically a product property arising due to combination of magnetostrictive (magnetic/mechanical) phenomena in ferrite and piezoelectric (meachanical/electrical) phenomena of ferroelectric phases [7].

Low value of ME coupling in single phase materials as compared to their ME composite counterparts, opens wider prospects for evolution of the latter. In late years, focus has been laid on synthesis and development of lead-free ME composites, due to environmental and health related concerns posed by lead-based ME composites. Distinct lead-free composites comprising

* Corresponding author.
E-mail: deepyogesh@gmail.com

of $BaFe_{12}O_{19}$ as a constituent phase including $0.9BaTiO_3$–$0.1Ba_{(1-x)}Sr_xFe_{12}O_{19}$ [8], $0.5BaFe_{12}O_{19}$–$0.5Na_{0.5}Bi_{0.5}TiO_3$ [9], $BaTiO_3$–$BaFe_{12}O_{19}$ [10], $Na_{0.5}Bi_{0.5}TiO_3$–$BaFe_{12}O_{19}$ [11], $(BaFe_{11.9}Al_{0.1}O_{19})_{1-x}$–$(BaTiO_3)_x$ [12], etc. are studied in the previous years. Generally for fabrication of good ME composites, the piezoelectric and magnetostrictive coefficients of constituent ferroelectric and ferrite phases should be high respectively. Furthermore high resistivity is equally desirable for avoiding leakage of charges [13].

$K_{0.5}Na_{0.5}NbO_3$ (KNN) has been considered as a bright prospect as a ferroelectric constituent for fabrication of lead-free ME composites. KNN exhibits reasonably well ferroelectric, piezoelectric, and dielectric characteristics. It exhibits high piezoelectric charge constant ($d_{33} \approx$ 80–416 pC/N) and a high planar coupling coefficient ($k_P \approx$ 45%) [14–16]. It also exhibits large remnant polarization and coercive field (P_r = 21 μC/cm^2, E_c = 7.2 kV/cm, P_r = 20 μC/cm^2, and E_c = 8 kV/cm) [14,17]. The M-type hexaferrites are widely studied materials due to their unique physical properties. The hexagonal ferrites including $BaFe_{12}O_{19}$ (BHF) have magneto-plumbite structure. The crystal structure of BHF and diamagnetically doped BHF may be described by two space group viz. $P6_3/mmc$ (No. 194) and $P6_3mc$ (No. 186). The latter one is a non-centrosymmetric space group and is generally used to describe the crystal structure in order to explain the existence of non-zero spontaneous polarization [18,19]. These ferrites are usually termed as hard ferrites because of their high electrical resistivity, saturation magnetization, coercivity, and mechanical hardness [20]. At higher frequencies, hexaferrites have low-eddy current losses and high resistivity as compared to other magnetic materials [21]. Substitution of Fe with any diamagnetic cation like In^+ in BHF can reduce the Curie temperature (T_c) and specific magnetization, thereby facilitating their use in various applications including multiple state memory elements, sensors, transducers, etc. [22,23]. Moreover, a large spontaneous polarization and enhanced multiferroic properties are recently observed in single phase BHF substituted by diamagnetic cations and the magnetoelectric characteristics of M-type hexaferrites synthesized by a modified ceramic technique are found to be more advanced than those obtained for well known room-temperature $BiFeO_3$ orthoferrite multiferroic [24–27]. Also they are ferrimagnetic systems having larger magnetostrictive nature [28]. Also very few reports are available on the ME composites having BHF as ferrite phase and KNN as ferroelectric phase. Keeping the above facts in mind we were motivated to fabricate and study the different properties of $(1-x)K_{0.5}Na_{0.5}NbO_3$–$(x)BaFe_{12}O_{19}$ (x = 30, 40, and 50 wt%) ME composites having KNN and BHF as constituent ferroelectric and ferrite phase respectively.

2 Experimental details

Novel lead-free ME composites viz. $(1-x)$KNN–(x)BHF (x = 30, 40, and 50 wt%) have been synthesized using solid state reaction method. Initially the KNN phase has been synthesized using solid state reaction method. The detailed procedure of synthesis is reported elsewhere [29]. Ferrite phase (BHF) has been synthesized with sol-gel method, employing barium nitrate $Ba(No_3)_2$, ferric nitrate $Fe(NO_3)_3 \cdot 9H_2O$, citric acid, and ethylene glycol as starting materials. Initially barium nitrate and ferric nitrate are mixed in appropriate molar proportions in aqueous solution of citric acid prepared in distilled water. The mixture is continuously stirred at 80 ℃ to get a homogeneous solution. Then ethylene glycol is added to the solution with a proportion of citric acid/ethylene glycol in the ratio of 70:30. This solution is then transformed into xerogel, which starts to swell, thereby producing a foamy precursor. The obtained xerogel is then dried in hot air oven at 120 ℃ for 12 h. The obtained powder from xerogel is then presintered at 900 ℃ for 3 h in air atmosphere to obtain the desired ferrite phase . The desired $(1-x)$KNN–(x)BHF ME composites have been synthesized by mixing the obtained KNN and BHF powders in different weight percentage ratios: 70:30, 60:40, and 50:50. The obtained composite powders have been shaped in the form of cylindrical pellets (of 10 mm diameter and thickness varying between 1 and 2 mm) using hydraulic press and then sintered in air atmosphere at optimized temperature of 1050 ℃ for 3 h.

Phase formation and structural characterizations of the composites have been examined with XRD patterns obtained from Bruker D8 X-ray diffractometer with Cu Kα radiation (λ = 1.5432 Å). Field emission scanning electron microscope (FE-SEM), Carl Zeiss has been used to study the surface morphology and microstructures of the composites. The room temperature magnetic and polarization hysteresis of the composites has been studied with vibrating sample magnetometer (VSM) Quantum Design, PAR 15, and Marine India automatic

P–E loop tracer respectively. Dielectric and impedance analysis of the composites has been performed using HIOKI-3532-50 Hi tester LCR meter. Presence of ME coupling in the composite samples is examined by measuring ME voltage coefficient (α_{ME}) dynamically [30].

3 Results and discussion

3. 1 Phase identification and microstructure

Figure 1 exhibits the XRD patterns of the (1−*x*)KNN–(*x*)BHF (*x* = 30, 40, and 50 wt%) composite samples. XRD peak indexing for composite samples agrees with reported KNN [29] having perovskite orthorhombic structure with space group *Amm*2 and BHF (JCPDS card 84-0757) having hexagonal structure with space group $P6_3/mmc$. XRD patterns of the composite samples assert that all the peaks corresponding to both the constituent phases are present and absence of impurity traces, confirming that both the constituent phases have retained their identity in the composites, thereby confirming their efficacious synthesis. We have prepared $K_{0.5}Na_{0.5}NbO_3$ and $BaFe_{12}O_{19}$ separately and then mixed the individual phases in required stoichiometry to synthesize the required composite system. So, there is no such oxygen excess or deficit in our samples. Oxygen vacancies are generally created when we substitute subvalent or supervalent cations. This process causes charge imbalance in the host lattice. This charge imbalance is then compensated by creation of oxygen vacancies. Since our synthesis does not involve any such substitution, we do not have oxygen vacancies in our system. The lattice parameters of the composite samples and their constituent phases are listed in Table 1. We do not observe any particular trend for the unit cell parameters with the concentration of individual phases as the composite systems were synthesized from the separately prepared individual phases mixed in the required stoichiometry. We have calculated the unit cell volume of the individual phases in the composites. At room temperature, the unit cell volume of the KNN phase in the prepared composites is found to be slightly less (0.28%–1.96%) than the unit cell volume of separate KNN phase with addition of BHF. The similar behaviour was also observed by Trukhanov *et al*. [31]. Surface morphology of the composite samples has been investigated using FE-SEM. Figure 2 displays FE-SEM micrographs of the composite samples along with their constituent phases. All the composites exhibit homogeneous microstructure. These micrographs confirm the formation of desired composites comprising of both the grains of the constituent phases. It is evident from the micrographs that composites comprise of two distinct phases viz. small hexagonal shaped grains akin to BHF phase and large polygonal shaped grains akin to KNN phase. Average grain size of the composite samples has been computed with Image J software and fitted using log-normal distribution and tabulated in Table 1. Figure 3 exhibits plots of grain size distribution with insets showing the obtained grain sizes.

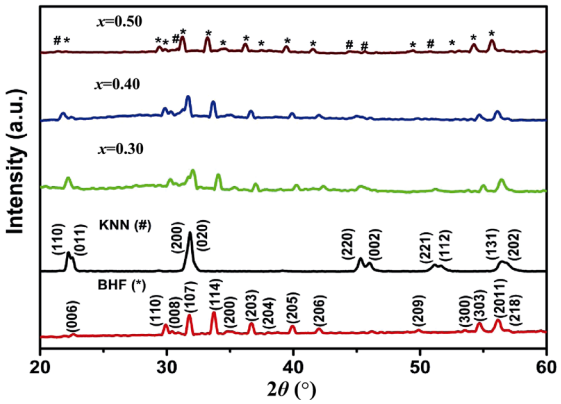

Fig. 1 XRD patterns of (1−*x*)KNN–(*x*)BHF (*x* = 30, 40, and 50 wt%) composites along with pure KNN and BHF phases where # represents KNN and * represents the BHF phase.

Table 1 Lattice parameters and average grain size of (1−*x*)KNN–(*x*)BHF (*x* = 30, 40, and 50 wt%) composites

Composition (*x*)	Lattice parameter (Å)					Average grain size (nm)
	BHF		KNN			
	a	*c*	*a*	*b*	*c*	
KNN	—	—	5.675	5.626	3.948	538.53
0.30	5.086	23.328	5.656	5.599	3.963	345.53
0.40	5.037	23.299	5.622	5.575	3.957	317.36
0.50	5.105	23.434	5.781	5.712	3.981	301.89
BHF	5.159	23.596	—	—	—	231.93

3. 2 Dielectric and impedance studies

The behaviour of dielectric constant (ε') of the (1−*x*)KNN–(*x*)BHF (*x* = 30, 40, and 50 wt%) composite samples is studied with temperature at three distinct frequencies (1, 5, and 10 kHz) in the temperature range of 30–500 ℃. Figure 4 exhibits the temperature dependence of dielectric constant of the composite samples along with their constituent phases. The ferroelectric (KNN) phase exhibits two transition peaks with first peak appearing in temperature range of 170–200 ℃ akin to

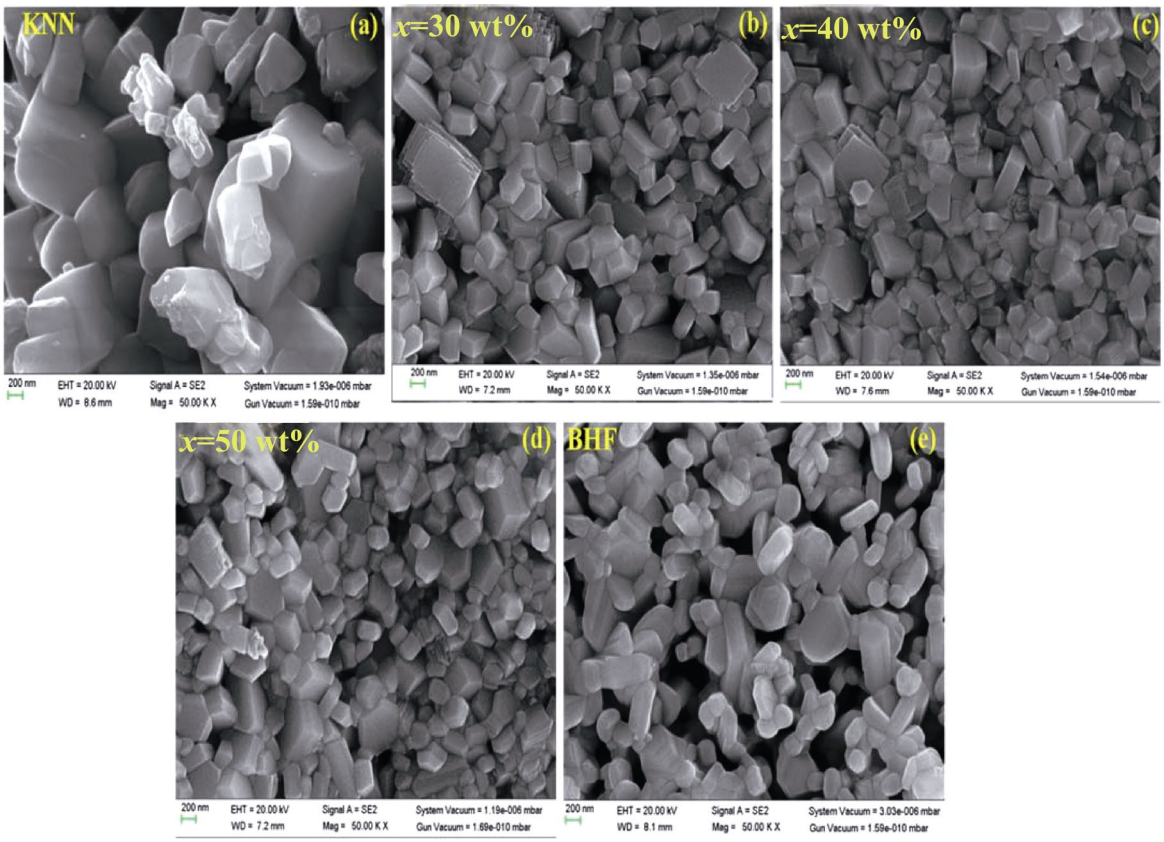

Fig. 2 FE-SEM micrographs of (1−*x*)KNN–(*x*)BHF composites: (a) KNN, (b) *x* = 30 wt%, (c) *x* = 40 wt%, (d) *x* = 50 wt%, and (e) BHF.

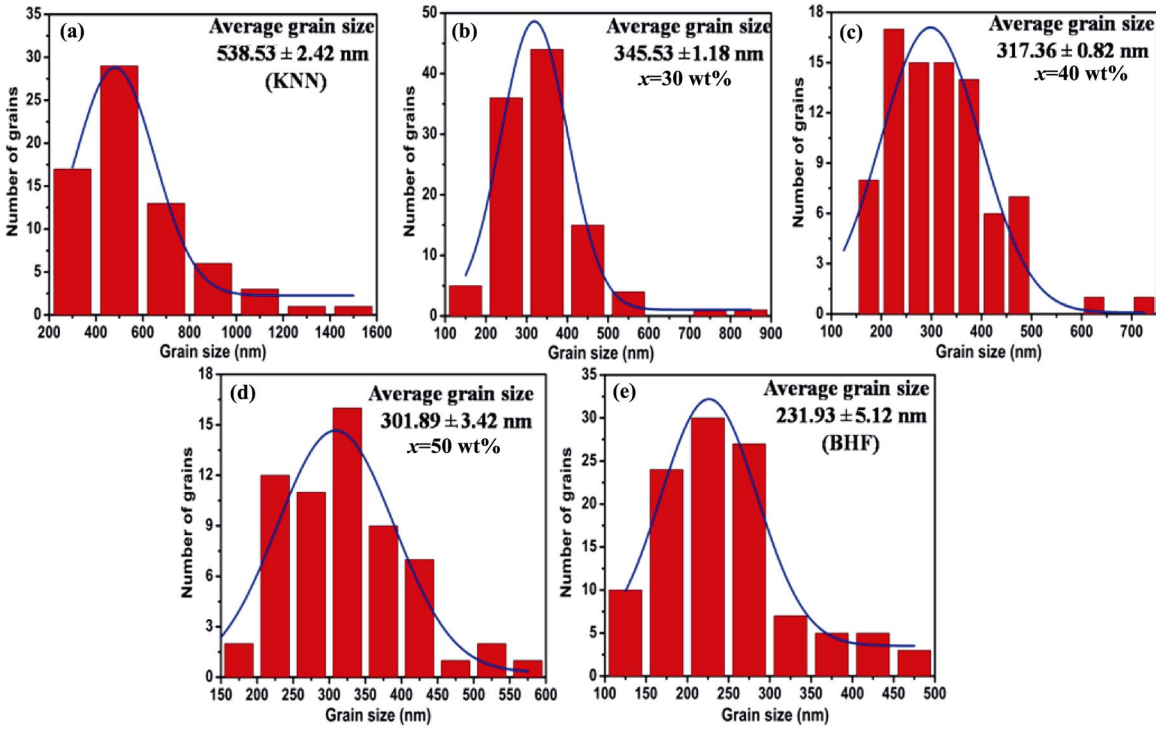

Fig. 3 Log normal distribution of grain size of (1−*x*)KNN–(*x*)BHF composites: (a) KNN, (b) *x* = 30 wt%, (c) *x* = 40 wt%, (d) *x* = 50 wt%, and (e) BHF. The insets represent the average grain sizes obtained.

orthorhombic–tetragonal phase transition (T_{O-T}) and second peak in the high temperature range of 420–440 ℃ akin to tetragonal–cubic phase transition (T_C) [29]. The temperature dependence of dielectric constant for ferrite (BHF) phase comprises of first transition peak in the range of 150–190 ℃ and the second transition peak which appears at ~455 ℃ corresponds to ferroelectric–paraelectric like phase transition. When electric field is applied to BHF, a huge number of dipoles are formed owing to inter ionic hopping via oxygen, giving it a ferroelectric character [32]. The plot of ε' vs. T of BHF has been divided into three regions as shown in Fig. 4(e). The compositional disorder in the crystal structure gives rise to formation of polar region [33], thereby affecting the dielectric behaviour. In region I the polar region remains frozen at lower temperatures and ε' increases with temperature. The increase in temperature initiates the conversion of big polar region to nano size polar regions in order to minimize the thermal energy. During this process, ε' starts to decrease as evident from region II of Fig. 4(e) giving rise to first peak (T_r). This in particular indicates the relaxor type characteristic of the sample and is not a phase transition. After this, ε' again increases with temperature owing to the existence of large number of nano polar regions. In the nano polar region, electric dipoles require lower energy to be polarized, thereby giving rise to high ε' between regions II and III. On increasing the temperature further, the ordered electric dipoles become disordered owing to surplus of thermal energy consequently causing a sudden decrease in ε' with temperature increases. This peak temperature corresponds to ferroelectric–paraelectric phase transition (T_m) [34]. The obtained results are nearly consistent with Ref. [35]. Both T_r and T_C are found to increase slightly with frequency. It is interesting to note that BHF exhibits multiferroic character [36,37]. Therefore we can not neglect the magnetic phase transition (ferro–paramagnetic) of BHF, which occurs at ~445 ℃ and others appear at around 130 ℃. These transitions in BHF require further study by measuring temperature dependent magnetization. Figures 4(b)–4(d) show that the composite samples exhibit transition peaks corresponding to both the constituent phases which are marked by their corresponding symbol in the respective plots. It is evident from Fig. 4 that ε' decreases with addition of BHF weight percentage in the composites. This may be accounted for a decrease in grain size with addition of BHF in the composite samples. It is assumed that the ferroelectric phase has large number of ferroelectric domains separated from each other by domain walls. Number of domain walls and their mobility affect ε' [38]. From the point of view of Okazaki and Nagata [39], the grain boundaries and domain walls comprise of space charge sites in a certain amount. These sites are responsible for producing electric field which significantly affects domain wall mobility. When the grain size decreases it leads to an increase in surface area of space charge layer, consequently enhancing the space charge field. As a result of this the domain wall motion becomes comparatively arduous and non uniform which is responsible for decrease in ε'. Figure 5 exhibits the variation of dielectric constant (ε') with frequency for the composite samples at room temperature in the frequency range of 50 Hz–1 MHz. ε' is found to decrease over whole frequency range having very subtle changes in the high frequency regime. This type of behaviour in composites may be attributed to Maxwell–Wagner interfacial polarization [40,41] which gives rise to uncompensated charges at the interface separating two constituent phases of the composites. Grains are less resistive as compared to grain boundaries, thereby favouring the gathering of electrons at grain boundaries on application of external AC field giving rise to space charge polarization. This accounts for higher values of ε' at lower frequencies. With increase in frequency further the electrons are not able to align with the frequency of applied field, consequently decreasing the ε' at higher frequencies. Magnitude of ε' is found to decrease with increasing BHF content of x = 30–50 wt%. Similar behaviour of ε' has been reported by Trukhanov *et al*. [42–44] for diamagnetic substitution in BHF.

The temperature dependent complex impedance spectra, Z'' vs. Z' known as Nyquist plot are shown in Figs. 6(a)–6(c) for the $(1-x)$KNN–(x)BHF composites. Two semicircular arcs are obtained at distinct temperatures (30, 50, and 100 ℃). The high and low frequency semicircular arcs signify the presence of bulk (grain) and grain boundary contributions respectively. Bulk contribution mainly arises by parallel integration of bulk resistance and capacitance (R_b and C_b), while grain boundary contribution comes into playing with parallel combination of grain boundary resistance and capacitance (R_{gb} and C_{gb}) respectively. Both R_b and R_{gb} can be directly obtained from the intercepts of the semicircular arcs on the abscissa axis of Nyquist plots. It is evident from Fig. 6 that both R_g and R_{gb} are found

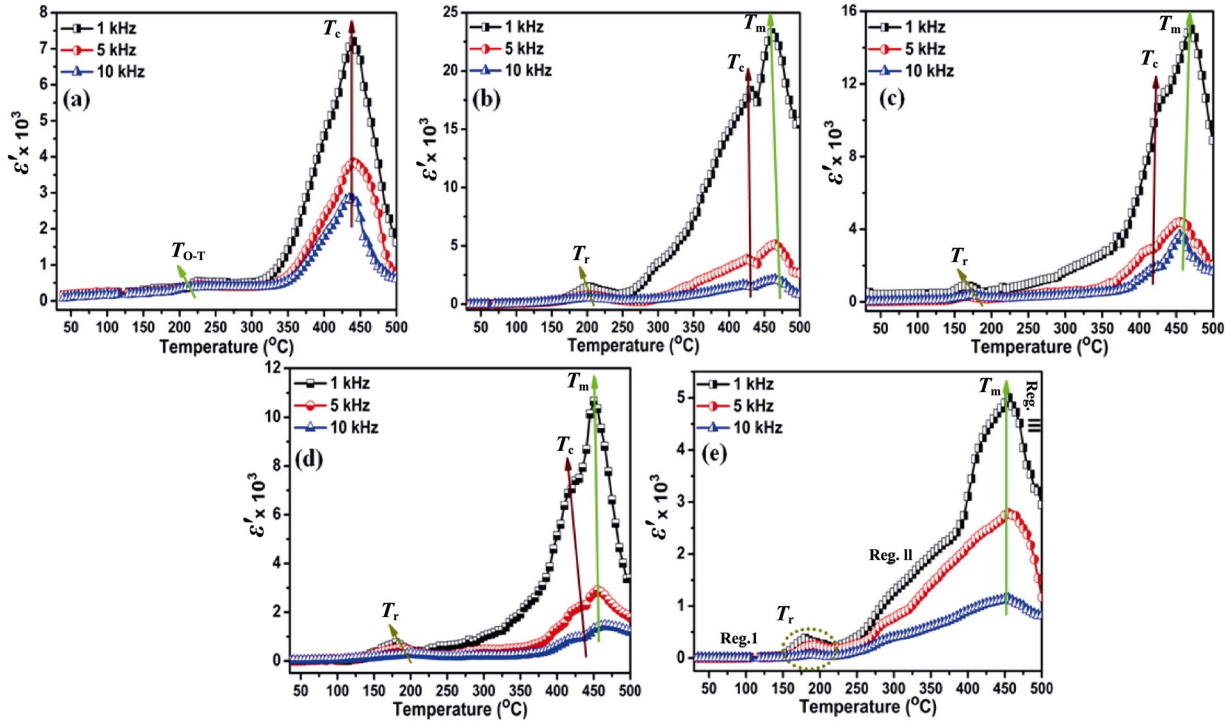

Fig. 4 Temperature dependence of dielectric constant (ε') for (1−x)KNN–(x)BHF composites: (a) KNN, (b) x = 30 wt%, (c) x = 40 wt%, (d) x = 50 wt%, and (e) BHF.

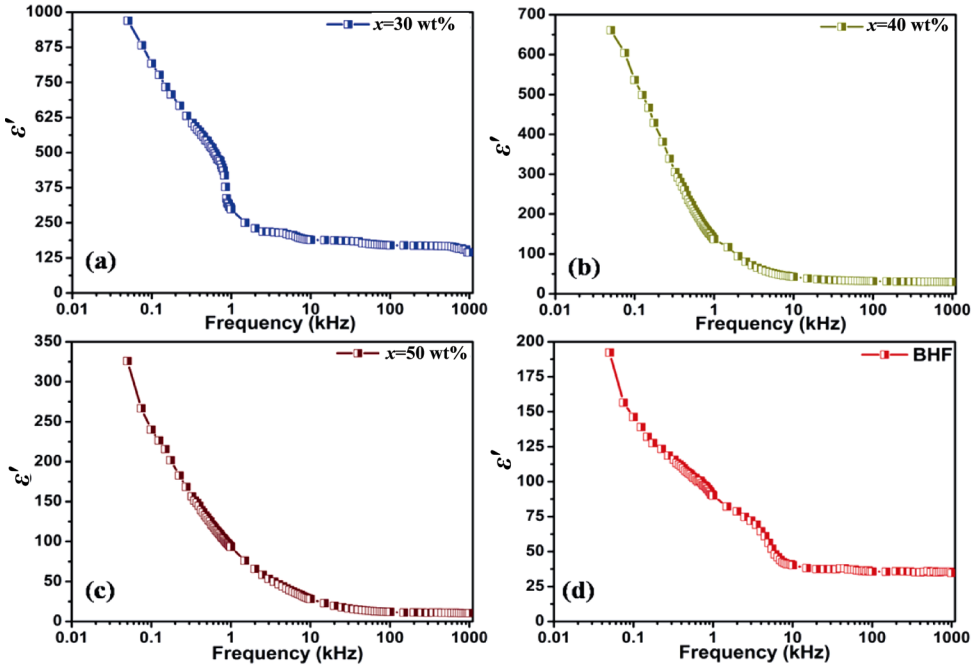

Fig. 5 Frequency dependence of dielectric constant (ε') for (1−x)KNN–(x)BHF composites: (a) x = 30 wt%, (b) x = 40 wt%, (c) x = 50 wt%, and (d) BHF.

to decrease with increase in temperature confirming the negative temperature coefficient of resistance (NTCR) behaviour of the composites analogous to the semiconductors [45]. It is also observed that all the semicircles exhibit some degree of depression signalling that the centre of these semicircles lies below the abscissa axis, indicating presence of non-Debye type of relaxation phenomena in the composite samples. Figure 6(d) exhibits the Nyquist plots of (1−x)KNN–(x)BHF (x = 30, 40, and 50 wt%) composites at room temperature signalling the decrease in impedance with addition of BHF weight percentage in the composites.

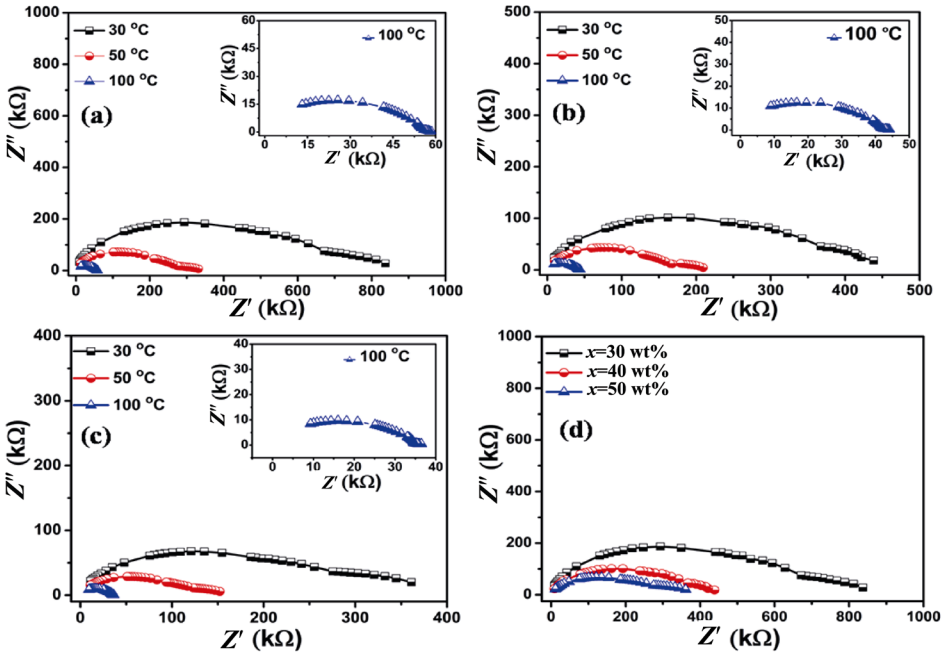

Fig. 6 Complex impedance spectra of (1−*x*)KNN–(*x*)BHF composites: (a) *x* = 30 wt%, (b) *x* = 40 wt %, (c) *x* = 50 wt%, and (d) complex impedance spectra of (1−*x*)KNN–(*x*)BHF (*x* = 30, 40, and 50 wt%) composites at room temperature.

Figures 7(a)–(c) show the variation of imaginary part of electric modulus with frequency for (1−*x*)KNN–(*x*) BHF (*x* = 30, 40, and 50 wt%) composites at different temperatures. From *f* vs. M'' plots, the variation of M'' as a function of frequency is characterized by: (a) appearance of peaks at a particular frequency at different temperatures and (b) peaks shift towards higher frequency side with increase in temperature. The lower frequency regime on left side of peak indicates the frequency range for which the charge carriers are capable of moving over a long distance, which means they can perform hopping from one site to neighbouring site easily [46]. The higher frequency regime on right side of peak denotes the frequency range for which the charge carriers remain spatially restricted to their potential wells and perform localized motion with in the well [47]. Appearance of peak in the modulus spectrum indicates the transition from long range to short range mobility with enhancement in frequency. Moreover, it also indicates the conductivity relaxation in the composites. Shifting of peaks towards higher frequency regime with increase in temperature indicates a thermally activated relaxation process in which charge carrier hopping with small polarons is dominated intrinsically for all compounds [48].

3. 3 Ferroelectric studies

The ferroelectric ordering in the composite samples has been established from *P*–*E* hysteresis loops. Figures 8(a)–8(e) exhibit the *P*–*E* hysteresis loops of pure KNN and BHF phases along with that of (1–*x*)KNN–(*x*)BHF (*x* = 30, 40, and 50 wt%) composites obtained at 50 Hz frequency and at room temperature.

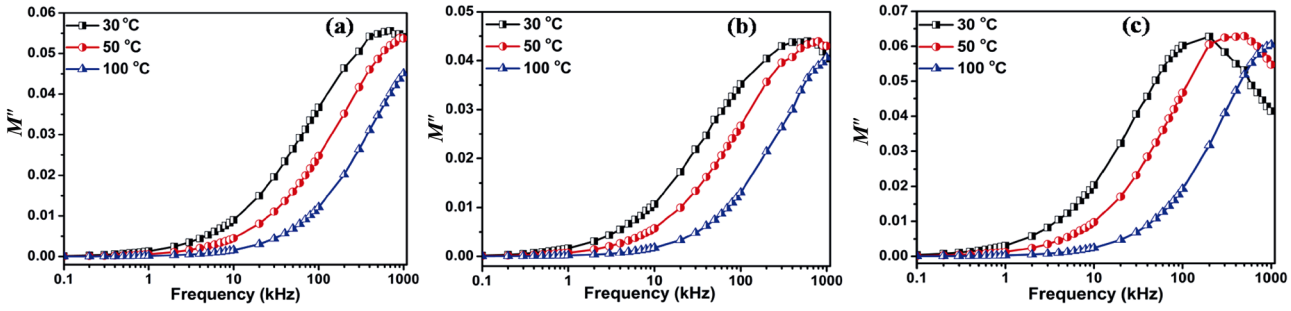

Fig. 7 Variation of imaginary part (M'') of modulus with frequency for (1−*x*)KNN–(*x*) BHF composites: (a) *x* = 30 wt%, (b) *x* = 40 wt%, and (c) *x* = 50 wt%.

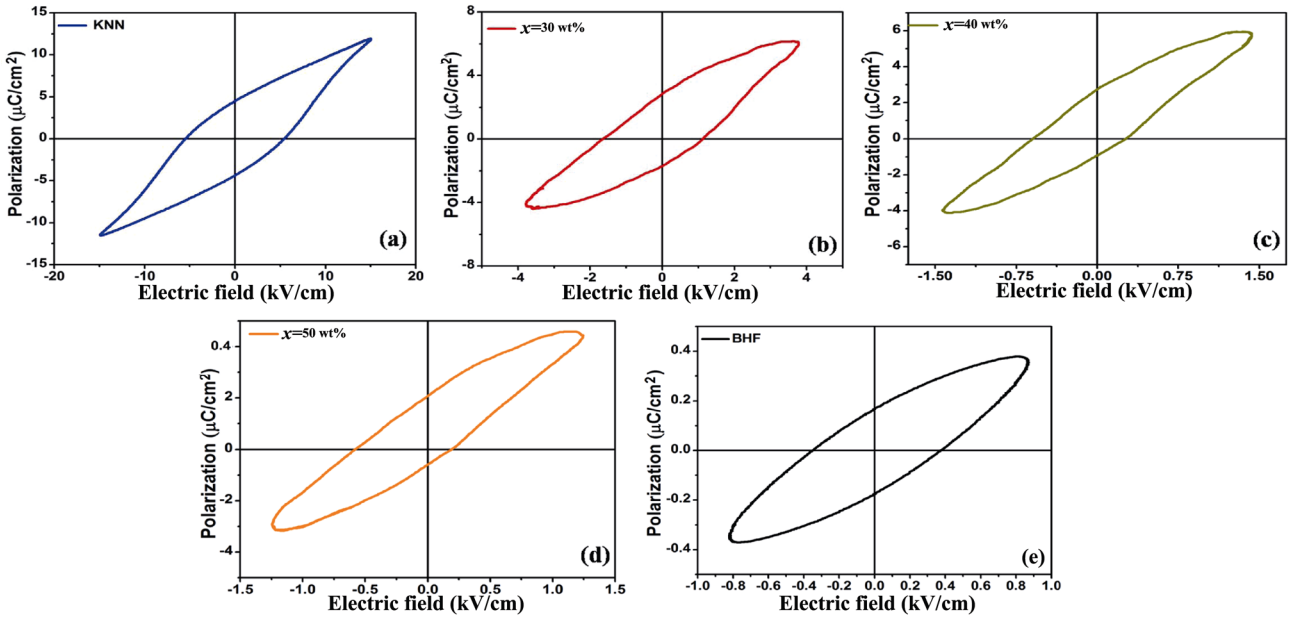

Fig. 8 *P–E* hysteresis loops for (1−*x*)KNN–(*x*)BHF composites obtained at room temperature: (a) KNN, (b) *x* = 30 wt%, (c) *x* = 40 wt%, and (d) *x* = 50 wt%.

The polarization in BHF may be attributed to the change in the central position of Fe in the FeO_6 octahedron of the subunit cell of BHF. Generally Fe is found at the centre of octahedron. When an external field is applied, it gives rise to off center shift for Fe, thereby inducing electric polarization [49]. Remnant polarization (P_r) of the composites is found to decrease with BHF weight percentage. This may be attributed to enhancement in conductivity, consequently increasing the leakage current. This behaviour may also be correlated with the Nyquist plots obtained for the composites (Fig. 6(d)) which can provide information about resistance by calculating the intercept made by semicircular arcs on the abscissa axis of Nyquist plots. The resistance is found to decrease with increase in BHF weight percentage, thereby reducing the electro-mechanical coupling which consequently lowers P_r [50].

3. 4 Magnetic studies

The magnetic characteristics of the (1−*x*)KNN–(*x*)BHF (*x* = 30, 40, and 50 wt%) composites are studied using *M–H* hysteresis loops at room temperature at an applied magnetic field of −10 kOe $\leqslant H \leqslant$ 10 kOe. Figures 9(a) and 9(b) exhibit the *M–H* hysteresis loops of the composites along with pure BHF phase. As evident from Fig. 9 that composite samples and pristine BHF exhibit rapid increase in magnetization at lower fields which further slows down at higher fields and they either do not show saturation in magnetization in the applied field range. The saturation magnetization (M_s) of the composites is approximated using law of saturation [51–53] employing following relation between magnetization (M) and magnetic field (H) given by Eq. (1):

$$M(H) = M_s\left(1+\frac{A}{H}+\frac{B}{H^2}\right)+\chi_P H \qquad (1)$$

where M_s is the saturation magnetization, χ_P is the high field susceptibility, A/H is related with inhomogeneities and usually neglected at higher magnetic field, and B/H^2 is related to magnetocrystalline anisotropy [53]. The saturation magnetization is computed using Eq. (1) (Table 2) and found to increase with addition of BHF in the composite samples. The coercive field (H_c) of the composite samples is also estimated from the *M–H* hysteresis loops (Table 2) and found to decrease with increase in BHF weight percentage. The variation of M_s and H_c with BHF content is shown in Fig. 9(c). Individual grains of ferrite in the composite samples act as magnetization centres. The net magnetization arises from sum of these individual contributions. The ferrite addition in the composites strongly enhances the magnetic contacts, consequently increasing the net magnetization [54]. The decreasing trend of H_c may be attributed to the change of easy axis of magnetization from *c*-axis to basal plane which may lower the anisotropic field (H_a) [11,55]. For hexagonal ferrites, the aniosotropic parameter is given using Eq. (2) [56]:

$$B = -\frac{1}{15} \times {H_a}^2 \quad (2)$$

where H_a is the anisotropy field, expressed using Eq. (3) [57]:

$$H_a = \frac{2K_1}{M_s} \quad (3)$$

where K_1 is the first order anisotropy constant and M_s is the saturation magnetization.

Combining Eqs. (1) and (3), we get the following equation

$$M(H) = M_s\left(1 - \frac{4{K_1}^2}{15{M_s}^2H^2}\right) + \chi_P H \quad (4)$$

The anisotropy field H_a is estimated using Eqs. (3) and (4) and tabulated in Table 1. Since H_a is proportional to H_c, so analogous to H_c, H_a also follows the same trend as expected and is found to reduce with addition of BHF (Fig. 9(d)). This may be attributed to growth of interface magnetization at KNN–BHF interfaces which act as reverse pinning effect [58].

Table 2 Magnetic parameters of(1–*x*)KNN–(*x*)BHF (*x* = 30, 40, and 50 wt%) composites

Composition (*x*)	H_c (kOe)	H_a (kOe)	M_s (emu/g)
BHF	5.30	31.55	71.52
0.30	2.96	28.84	49.54
0.40	2.28	26.75	55.87
0.50	1.63	25.49	60.87

In order to understand more about magnetic ordering, the temperature dependent magnetization of BHF phase was obtained at a magnetic field of 1 kOe in the temperature range of 5–300 K as shown in Fig. 9(e). The measurements are taken in zero field cooled (ZFC) and field cooled (FC) modes. In ZFC mode, we cooled the samples in absence of magnetic field up to 5 K and then a magnetic field of 1 kOe was applied. Then we measured the magnetization while heating the samples from 5 to 300 K. In FC mode, we cooled the sample in the presence of magnetic field of 1 kOe up to 5 K and then measured the magnetization while heating the sample from 5 to 300 K in the presence of magnetic field. The main features of *M*–*T* curve of BHF as evident from Fig. 9(e) are: (i) large irreversibility among ZFC and FC magnetizations and (ii) presence of wide maxima (cusp) in ZFC magnetization. The irreversibility between ZFC and FC magnetizations indicates the absence of long range ferromagnetic ordering. The ZFC curve exhibits a broad maxima around 50 K, whereas FC exhibits almost temperature independent behaviour below this temperature. The cusp like or broad maxima behaviour of the composites indicates the presence of spin glass behaviour as reported earlier [59]. This is generally attributed to randomness of neighbouring coupling or magnetic moments and mixed interactions which results in frustration. The similar behaviour is also observed for (1–*x*)KNN–(*x*)BHF (*x* = 30, 40, and 50 wt%) composites.

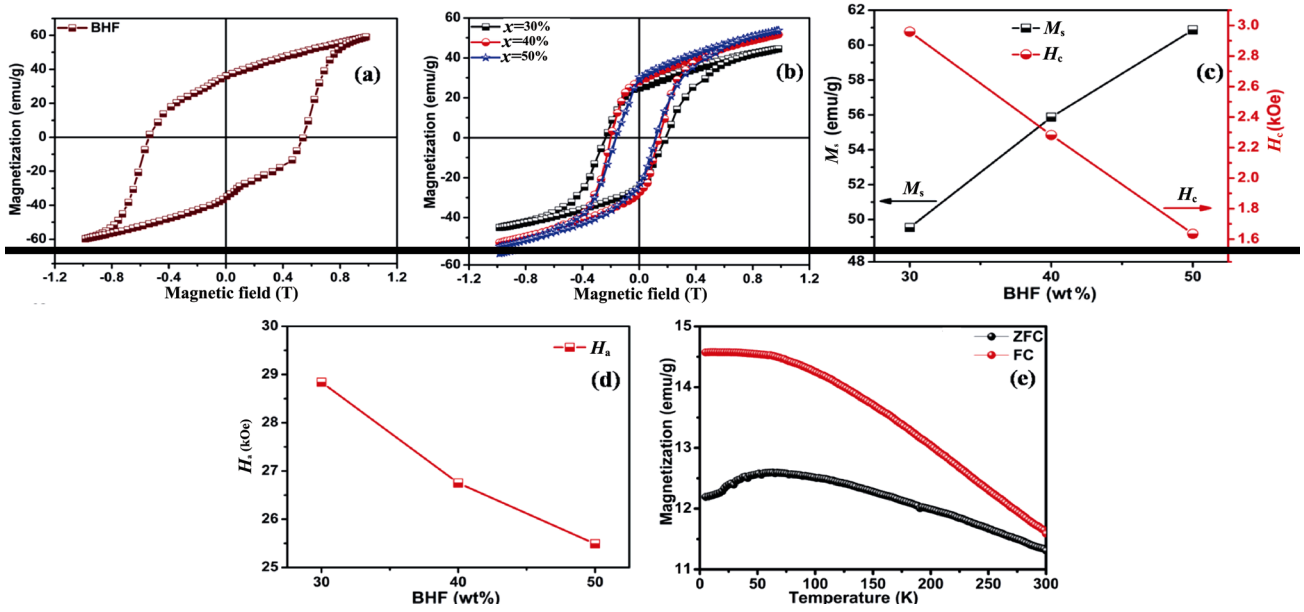

Fig. 9 *M*–*H* hysteresis loops for (a) BHF, (b) (1−*x*)KNN–(*x*)BHF (*x* = 30, 40, and 50 wt%) composites, (c) variation of saturation magnetization (M_s) and coercive field (H_c), (d) anisotropy field (H_a) of composites with BHF weight percentage, and (e) magnetization vs. temperature plot for pure BHF.

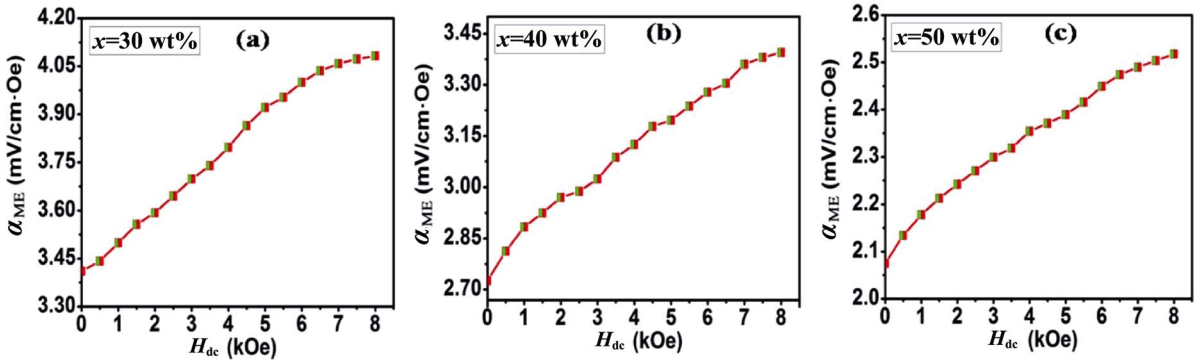

Fig. 10 Variation of α_{ME} with DC magnetic field for (1−*x*)KNN–(*x*)BHF composites at room temperature: (a) *x* = 30 wt%, (b) *x* = 40 wt%, and (c) *x* = 50 wt%.

3. 5 Magnetoelectric studies

ME voltage coefficient (α_{ME}) has been determined using dynamic method [30] for establishing the ME coupling in the (1−*x*)KNN–(*x*)BHF (*x* = 30, 40, and 50 wt%) composites. Before measuring α_{ME}, the composite samples are electrically poled with ~1 kV·mm^{-1} of applied electric field for 1 h at 100 ℃. α_{ME} is then computed using Eq. (5) by applying a 5 Oe AC magnetic field having a frequency of 999 Hz while varying the DC magnetic field from 0 to 8000 Oe.

$$\alpha_{ME} = \frac{V_{out}}{t \times H_{ac}} \tag{5}$$

where V_{out} is the output voltage induced in the sample, *t* is the thickness of composite sample, and H_{ac} is the AC magnetic field used.

Figure 10 exhibits the behaviour of α_{ME} with DC magnetic field for the composites. The highest value of α_{ME} = 4.08 mV/(cm·Oe) is achieved for composite having *x* = 30 wt% of BHF. α_{ME} is found to increase with application of DC magnetic field and highest value is obtained at 8 kOe. Identical behaviour of α_{ME} is also reported earlier [60,61]. It is also evident from Fig. 10 that α_{ME} is found to decrease with addition of BHF. This is generally due to low resistivity of ferrite (BHF) phase as compared to ferroelectric (KNN) phase. Also with increase in BHF weight percentage, the effective poling of the composite samples becomes tedious due to leakage of charges through low resistive ferrite grains leading to enhancement in conduction at the BHF–KNN interfaces, thereby hampering the polarization consequently decreasing α_{ME} with addition of BHF [62]. Therefore, (1–*x*)KNN– (*x*)BHF (*x* = 30, 40, and 50 wt%) composites exhibit ME coupling with maximum α_{ME} = 4.08 mV/(cm·Oe) achieved for composite having *x* = 30 wt% of BHF.

4 Conclusions

Novel lead-free ME composites (1−*x*)KNN–(*x*)BHF (*x* = 30, 40, and 50 wt%) have been successfully synthesized using solid state reaction method. FE-SEM micrographs asserted the existence of both the individual phases and the average grain size varies between 232 and 540 nm. Dielectric properties of the composites were studied as a function of temperature and the dielectric constant of the composites was found to decrease with BHF weight percentage. P_r of the composites was found to reduce with BHF weight percentage. Magnetization of the composites was found to enhance with addition of BHF unlike coercive and anisotropy field which decrease with BHF weight percentage. The highest value of α_{ME} = 4.08 mV/(cm·Oe) was achieved for composite having *x* = 30 wt% of BHF. The substantial ME response of the composites may be exploited for potential applications in multifunctional devices.

Acknowledgements

Yogesh Kumar is thankful to MHRD, Government of India, New Delhi for providing research fellowship.

References

[1] Wang YJ, Li JF, Viehland D. Magnetoelectrics for magnetic sensor applications: Status, challenges and perspectives. *Mater Today* 2014, **17**: 269–275.

[2] Chappert C, Fert A, van Dau FN. The emergence of spin electronics in data storage. *Nature Mater* 2007, **6**: 813–823.

[3] Zhukov A, Ipatov M, Talaat A, *et al*. Studies of high-frequency giant magnetoimpedance effect in Co-rich amorphous microwires. *IEEE Trans Magn* 2015, **51**: 1–4.

[4] Palneedi H, Annapureddy V, Priya S, *et al*. Status and perspectives of multiferroic magnetoelectric composite materials and applications. *Actuators* 2016, **5**: 9.

[5] Surowiak Z, Bochenek D. Multiferroic materials for sensors, transducers and memory devices. *Arch Acoust* 2008, **33**: 243–260.

[6] Das J, Song YY, Wu MZ. Electric-field control of ferromagnetic resonance in monolithic $BaFe_{12}O_{19}$–$Ba_{0.5}Sr_{0.5}TiO_3$ heterostructures. *J Appl Phys* 2010, **108**: 043911.

[7] Nan CW, Bichurin MI, Dong SX, *et al*. Multiferroic magnetoelectric composites: Historical perspective, status, and future directions. *J Appl Phys* 2008, **103**: 031101.

[8] Gao ZY, Pu YP, Yao MT, *et al*. Superior electromagnetic properties obtained by enhanced resistivity on multiferroic barium titanate and hexaferrite di-phase composite ceramics. *Ceram Int* 2017, **43**: S85–S91.

[9] Pattanayak R, Muduli R, Panda RK, *et al*. Investigating the effect of multiple grain–grain interfaces on electric and magnetic properties of [50 wt% $BaFe_{12}O_{19}$–50 wt% $Na_{0.5}Bi_{0.5}TiO_3$] composite system. *Phys B*: *Condens Matter* 2016, **485**: 67–77.

[10] Srinivas A, Gopalan R, Chandrasekharan V. Room temperature multiferroism and magnetoelectric coupling in $BaTiO_3$-$BaFe_{12}O_{19}$ system. *Solid State Commun* 2009, **149**: 367–370.

[11] Pattanayak R, Raut S, Kuila S, *et al*. Multiferroism of [$Na_{0.5}Bi_{0.5}TiO_3$-$BaFe_{12}O_{19}$] lead-free novel composite systems. *Mater Lett* 2017, **209**: 280–283.

[12] Trukhanov SV, Trukhanov AV, Salem MM, *et al.* Preparation and investigation of structure, magnetic and dielectric properties of $(BaFe_{11.9}Al_{0.1}O_{19})_{(1-x)}$-$(BaTiO_3)_x$ bicomponent ceramics. *Ceram Int* 2018, **44**: 21295–21302.

[13] van den Boomgaard J, Born RAJ. A sintered magnetoelectric composite material $BaTiO_3$-Ni(Co, Mn) Fe_2O_4. *J Mater Sci* 1978, **13**: 1538–1548.

[14] Gao DJ, Kwok KW, Lin DM, *et al*. Microstructure and electrical properties of La-modified $K_{0.5}Na_{0.5}NbO_3$ lead-free piezoelectric ceramics. *J Phys D: Appl Phys* 2009, **42**: 035411.

[15] Guo YP, Kakimoto KI, Ohsato H. Phase transitional behavior and piezoelectric properties of $(Na_{0.5}K_{0.5})NbO_3$–$LiNbO_3$ ceramics. *Appl Phys Lett* 2004, **85**: 4121–4123.

[16] Li JF, Wang K, Zhu FY, *et al*. (K,Na)NbO_3-based lead-free piezoceramics: Fundamental aspects, processing technologies, and remaining challenges. *J Am Ceram Soc* 2013, **96**: 3677–3696.

[17] Rani J, Yadav KL, Prakash S. Modified structure and electrical properties of BSZT doped KNN hybrid ceramic. *Appl Phys A* 2012, **108**: 761–764.

[18] Trukhanov SV, Trukhanov AV, Turchenko VA, *et al*. Magnetic and dipole moments in indium doped barium hexaferrites. *J Magn Magn Mater* 2018, **457**: 83–96.

[19] Turchenko VA, Trukhanov SV, Balagurov AM, *et al*. Features of crystal structure and dual ferroic properties of $BaFe_{12-x}Me_xO_{19}$(Me = In^{3+} and Ga^{3+}; x = 0.1–1.2). *J Magn Magn Mater* 2018, **464**: 139–147.

[20] Ashima, Sanghi S, Agarwal A, *et al*. Rietveld refinement, electrical properties and magnetic characteristics of Ca-Sr substituted barium hexaferrites. *J Alloys Compd* 2012, **513**: 436–444.

[21] Ashiq MN, Iqbal MJ, Gul IH. Structural, magnetic and dielectric properties of Zr-Cd substituted strontium hexaferrite ($SrFe_{12}O_{19}$) nanoparticles. *J Alloys Compd* 2009, **487**: 341–345.

[22] Trukhanov SV, Trukhanov AV, Turchenko VA, *et al.* Crystal structure and magnetic properties of the $BaFe_{12-x}In_xO_{19}$ (x = 0.1–1.2) solid solutions. *J Magn Magn Mater* 2016, **417**: 130–136.

[23] Trukhanov SV, Trukhanov AV, Turchenko VA, *et al*. Structure and magnetic properties of $BaFe_{11.9}In_{0.1}O_{19}$ hexaferrite in a wide temperature range. *J Alloys Compd* 2016, **689**: 383–393.

[24] Trukhanov SV, Trukhanov AV, Kostishin VG, *et al*. Coexistence of spontaneous polarization and magnetization in substituted M-type hexaferrites $BaFe_{12-x}Al_xO_{19}$ (x < 1.2) at room temperature. *Jetp Lett* 2016, **103**: 100–105.

[25] Trukhanov AV, Trukhanov SV, Panina LV, *et al*. Strong corelation between magnetic and electrical subsystems in diamagnetically substituted hexaferrites ceramics. *Ceram Int* 2017, **43**: 5635–5641.

[26] Trukhanov AV, Trukhanov SV, Kostishin VG, *et al*. Multiferroic properties and structural features of M-type Al-substituted barium hexaferrites. *Phys Solid State* 2017, **59**: 737–745.

[27] Trukhanov SV, Trukhanov AV, Turchenko VA, *et al*. Polarization origin and iron positions in indium doped barium hexaferrites. *Ceram Int* 2018, **44**: 290–300.

[28] Pullar RC. Hexagonal ferrites: A review of the synthesis, properties and applications of hexaferrite ceramics. *Prog Mater Sci* 2012, **57**: 1191–1334.

[29] Kumar Y, Yadav KL, Manjusha, *et al*. Study of structural, dielectric, electric, magnetic and magnetoelectric properties of $K_{0.5}Na_{0.5}NbO_3$-$Ni_{0.2}Co_{0.8}Fe_2O_4$ composites. *Ceram Int* 2017, **43**: 13438–13446.

[30] Kumar MM, Srinivas A, Suryanarayana SV, *et al.* An experimental setup for dynamic measurement of magnetoelectric effect. *Bull Mater Sci* 1998, **21**: 251–255.

[31] Trukhanov SV, Trukhanov AV, Vasiliev AN, *et al.* Magnetic state of the structural separated anion-deficient $La_{0.70}Sr_{0.30}MnO_{2.85}$ manganite. *J Exp Theor Phys* 2011, **113**: 819–825.

[32] Tokunaga Y, Kanego Y, Okuyama D, *et al.* Multiferroic M-type hexaferrites with a room temperature conical state and magnetically controllable spin helicity. *Phys Rev Lett* 2010, **105**: 257201.

[33] Hiruma Y, Nagata H, Takenaka T. Detection of morphotropic phase boundary of $(Bi_{1/2}Na_{1/2})TiO_3$–$Ba(Al_{1/2}Sb_{1/2})O_3$ solid-solution ceramics. *Appl Phys Lett* 2009, **95**: 052903.

[34] Kumar S, Supriya S, Kar M. Correlation between temperature dependent dielectric and DC resistivity of Cr substituted barium hexaferrite. *Mater Res Express* 2017, **4**: 126302.

[35] Tan GL, Li W. Ferroelectricity and ferromagnetism of

M-type lead hexaferrite. *J Am Ceram Soc* 2015, **98**: 1812–1817.

[36] Tan GL, Chen XN. Structure and multiferroic properties of barium hexaferrite ceramics. *J Magn Magn Mater* 2013, **327**: 87–90.

[37] Kimura T, Lawes G, Ramirez AP. Electric polarization rotation in a hexaferrite with long-wavelength magnetic structures. *Phys Rev Lett* 2005, **94**: 137201.

[38] Shaw TM, Trolier-Mckinstry S, McIntyre PC. The properties of ferroelectric films at small dimensions. *Annu Rev Mater Sci* 2000, **30**: 263–298.

[39] Okazaki K, Nagata K. Effects of grain size and porosity on electrical and optical properties of PLZT ceramics. *J Am Ceram Soc* 1973, **56**: 82–86.

[40] Maxwell JC. *Electricity and Magnetism*. London: Oxford University Press, 1873.

[41] Wagner KW. The distribution of relaxation times in typical dielectrics. *Ann Phys* 1953, **40**: 817.

[42] Trukhanov SV, Trukhanov AV, Kostishyn VG, *et al*. Magnetic, dielectric and microwave properties of the $BaFe_{12-x}Ga_xO_{19}$ ($x \leqslant 1.2$) solid solutions at room temperature. *J Magn Magn Mater* 2017, **442**: 300–310.

[43] Trukhanov SV, Trukhanov AV, Kostishyn VG, *et al*. Investigation into the structural features and microwave absorption of doped barium hexaferrites. *Dalton Trans* 2017, **46**: 9010–9021.

[44] Trukhanov SV, Trukhanov AV, Kostishyn VG, *et al*. Effect of gallium doping on electromagnetic properties of barium hexaferrite. *J Phys Chem Solids* 2017, **111**: 142–152.

[45] Atamanik E, Thangadurai V. Study of the dielectric properties in the $NaNbO_3$–$KNbO_3$–In_2O_3 system using AC impedance spectroscopy. *Mater Res Bull* 2009, **44**: 931–936.

[46] Prasad K, Kumari Lily K, Chandra KP, *et al*. Electrical conduction in $(Na_{0.5}Bi_{0.5})TiO_3$ ceramic: Impedance spectroscopy analysis. *Adv Appl Ceram* 2007, **106**: 241–246.

[47] Pradhan DK, Choudhary RNP, Rinaldi C, *et al*. Effect of Mn substitution on electrical and magnetic properties of $Bi_{0.9}La_{0.1}FeO_3$. *J Appl Phys* 2009, **106**: 024102.

[48] Tiwari B, Choudhary RNP. Frequency-temperature response of $Pb(Zr_{0.65-x}Ce_xTi_{0.35})O_3$ ferroelectric ceramics: Impedance spectroscopic studies. *J Alloys Compd* 2010, **493**: 1–10.

[49] Kumar P, Gaur A. Signature of multiferroicity and pyroelectricity close to room temperature in $BaFe_{12}O_{19}$ hexaferrite. *Ceram Int* 2017, **43**: 16403–16407.

[50] Fawzi AS, Sheikh AD, Mathe VL. Dielectric, electrical and magnetoelectric characterization of $(x)Ni_{0.8}Zn_{0.2}Fe_2O_4$+ $(1-x)Pb_{0.93}La_{0.07}(Zr_{0.60}Ti_{0.40})O_3$ composites. *Mater Res Bull* 2010, **45**: 1000–1007.

[51] Grössinger R. Correlation between the inhomogeneity and the magnetic anisotropy in polycrystalline ferromagnetic materials. *J Magn Magn Mater* 1982, **28**: 137–142.

[52] Narang SB, Singh C, Yang B, *et al*. Microstructure, hysteresis and microwave absorption analysis of $Ba_{(1-x)}Sr_xFe_{12}O_{19}$ ferrite. *Mater Chem Phys* 2008, **111**: 225–231.

[53] Li ZW, Ong CK, Yang Z, *et al.* Site preference and magnetic properties for a perpendicular recording material: $BaFe_{12-x}Zn_{x/2}Zr_{x/2}O_{19}$ nanaoparticles. *Phys Rev B* 2000, **62**: 6530–6537.

[54] Devan RS, Chougule BK. Effect of composition on coupled electric, magnetic, and dielectric properties of two phase particulate magnetoelectric composite. *J Appl Phys* 2007, **101**: 014109.

[55] Kubo O, Ido T, Yokoyama H. Properties of Ba ferrite particles for perpendicular magnetic recording media. *IEEE Trans Magn* 1982, **18**: 1122–1124.

[56] Han MG, Ou Y, Chen WB, *et al*. Magnetic properties of Ba-M-type hexagonal ferrites prepared by the sol-gel method with and without polyethylene glycol added. *J Alloys Compd* 2009, **474**: 185–189.

[57] Ghasemi A, Morisako A. Static and high frequency magnetic properties of Mn–Co–Zr substituted Ba-ferrite. *J Alloys Compd* 2008, **456**: 485–491.

[58] Duan CG, Velev JP, Sabirianov RF, *et al*. Tailoring magnetic anisotropy at the ferromagnetic/ferroelectric interface. *Appl Phys Lett* 2008, **92**: 122905.

[59] Trukhanov SV, Trukhanov AV, Vasiliev AN, *et al*. Frustrated exchange interactions formation at low temperatures and high hydrostatic pressures in $La_{0.70}Sr_{0.30}MnO_{2.85}$. *J Exp Theor Phys* 2010, **111**: 209–214.

[60] Sharma A, Kotnala RK, Negi NS. Observation of multiferroic properties and magnetoelectric effect in $(x)CoFe_2O_4$–$(1-x)Pb_{0.7}Ca_{0.3}TiO_3$ composites. *J Alloys Compd* 2014, **582**: 628–634.

[61] Gupta R, Shah J, Chaudhary S, *et al*. Magnetoelectric coupling-induced anisotropy in multiferroic nanocomposite $(1-x)BiFeO_{3-x}BaTiO_3$. *J Nanopart Res* 2013, **15**: 2004.

[62] Duan CG. Interface/surface magnetoelectric effects: New routes to the electric field control of magnetism. *Front Phys* 2012, **7**: 375–379.